The Astronomical Journal, 162:251 (11pp), 2021 December https://doi.org/10.3847/1538-3881/ac29ba
© 2021. The American Astronomical Society. All rights reserved.

SCExAO/CHARIS Direct Imaging of A Low-mass Companion At A Saturn-like Separation from an Accelerating Young A7 Star

Jeffrey Chilcote[1], Taylor Tobin[1], Thayne Currie[2,3,4], Timothy D. Brandt[5], Tyler D. Groff[6], Masayuki Kuzuhara[7], Olivier Guyon[2,7,8,9], Julien Lozi[2], Nemanja Jovanovic[10], Ananya Sahoo[2], Vincent Deo[2], Eiji Akiyama[11], Markus Janson[12], Jill Knapp[13], Jungmi Kwon[14], Michael W. McElwain[6], Jun Nishikawa[7,14,15], Kevin Wagner[8,19], Krzysztof Hełminiak[16], Nour Skaf[2,17], and Motohide Tamura[7,14,18]

[1] Department of Physics, University of Notre Dame, South Bend, IN, USA; jchilcote@nd.edu
[2] Subaru Telescope, National Astronomical Observatory of Japan, 650 North A'ohōkū Place, Hilo, HI 96720, USA
[3] NASA-Ames Research Center, Moffett Boulevard, Moffett Field, CA, USA
[4] Eureka Scientific, 2452 Delmer Street Suite 100, Oakland, CA, USA
[5] Department of Physics, University of California, Santa Barbara, Santa Barbara, CA, USA
[6] NASA-Goddard Space Flight Center, Greenbelt, MD, USA
[7] Astrobiology Center of NINS, 2-21-1, Osawa, Mitaka, Tokyo, 181-8588, Japan
[8] Steward Observatory, The University of Arizona, Tucson, AZ 85721, USA
[9] College of Optical Sciences, University of Arizona, Tucson, AZ 85721, USA
[10] Department of Astronomy, California Institute of Technology, 1200 East California Boulevard, Pasadena, CA 91125, USA
[11] Department of Engineering, Niigata Institute of Technology, 1719 Fujihashi, Kashiwazaki, 945-1195, Japan
[12] Department of Astronomy, Stockholm University, AlbaNova University Center, 106 91 Stockholm, Sweden
[13] Department of Astrophysical Science, Princeton University, Peyton Hall, Ivy Lane, Princeton, NJ 08544, USA
[14] Department of Astronomy, Graduate School of Science, The University of Tokyo, 7-3-1, Hongo, Bunkyo-ku, Tokyo, 113-0033, Japan
[15] Department of Astronomical Science, School of Physical Sciences, The Graduate University for Advanced Studies (SOKENDAI), 2-21-1, Osawa, Mitaka, Tokyo, 181-8588, Japan
[16] Nicolaus Copernicus Astronomical Center, Polish Academy of Sciences, ul. Rabianska 8, 87-100 Torun, Poland
[17] LESIA, Observatoire de Paris, Université PSL, CNRS, Sorbonne Université, Université de Paris, 5 place Jules Janssen, F-92195 Meudon, France
[18] National Astronomical Observatory of Japan, 2-21-2, Osawa, Mitaka, Tokyo 181-8588, Japan
Received 2021 May 3; revised 2021 September 21; accepted 2021 September 22; published 2021 November 19

Abstract

We present the SCExAO direct imaging discovery and characterization of a low-mass companion to the nearby young A7IV star, HD 91312. SCExAO/CHARIS *JHK* (1.1–2.4 μm) spectra and SCExAO/HiCIAO *H*-band imaging identify the companion over a two year baseline in a highly inclined orbit with a maximum projected separation of 8 au. The companion, HD 91312 B, induces an 8.8σ astrometric acceleration on the star as seen with the Gaia & Hipparcos satellites and a long-term radial-velocity trend as previously identified by Borgniet et al. HD 91312 B's spectrum is consistent with that of an early-to-mid M dwarf. Hipparcos and Gaia absolute astrometry, radial-velocity data, and SCExAO/CHARIS astrometry constrain its dynamical mass to be $0.337^{+0.042}_{-0.044}$ $M_{\odot}$, consistent with - but far more precise than - masses derived from spectroscopy, and favors a nearly edge-on orbit with a semimajor axis of $\sim$9.7 au. This work is an example of precisely characterizing properties of low-mass companions at solar system-like scales from a combination of direct imaging, astrometry, and radial-velocity methods.

Unified Astronomy Thesaurus concepts: Direct imaging (387); Brown dwarfs (185); Coronagraphic imaging (313)

1. Introduction

Direct imaging and two *indirect* methods—radial-velocity (RV) and astrometry—provide ways to detect and characterize young exoplanets, brown dwarfs, and low-mass stellar companions at Jupiter or greater separations around nearby stars (Nakajima et al. 1995; Marois et al. 2008; Zimmerman et al. 2010; Brandt 2018; Borgniet et al. 2019; Brandt et al. 2019; Currie et al. 2020; Lagrange et al. 2020). Each method in isolation has its strengths and weaknesses. While direct imaging can probe key atmospheric properties—e.g., temperature, clouds, chemistry, and gravity—and provide some constraints on orbits, the masses this method derives are inferred from luminosity evolution models which themselves are uncertain. Furthermore, astrometric coverage from high-contrast direct imaging is usually small compared to the companion's likely orbital period (Currie et al. 2011; Spiegel & Burrows 2012; Carson et al. 2013; Kuzuhara et al. 2013; Barman et al. 2015; Berardo et al. 2017; Blunt et al. 2017; Lagrange et al. 2019). On the other hand, astrometry and RV by themselves provide constraints on orbital properties and lower limits on masses, but do not provide the same insight into atmospheric properties.

Combining direct imaging with astrometry and/or RV substantially improves our ability to characterize low-mass companions (Brandt et al. 2019). Relative astrometry of companions from imaging and absolute astrometry and/or Doppler light curves of the star can directly constrain companion masses and orbital properties. Atmospheric properties derived from imaging can be tied to the object's mass. The Hipparcos–Gaia Catalog of Accelerations (HGCA)—a combination of the exquisite astrometry from the Gaia mission and those from Hipparcos—provides a list of nearby stars whose proper-motion accelerations hint at the presence of massive, imageable companions on solar system scales (Brandt 2018; Gaia Collaboration et al. 2018). Direct imaging surveys targeting these accelerating stars may have significantly higher yields than blind surveys and allow substantially improved characterization capabilities (e.g., Calissendorff & Janson 2018;

[19] NASA Hubble Fellow.

Table 1
HD 91312 Observing Log

UT Date	Instrument	Coronagraph	Seeing (″)	Passband[a]	λ (μm)[a]	$t_{\rm exp}$ (s)	$N_{\rm exp}$	ΔPA (°)	PSF Subtraction Strategy
20161215	SCExAO/HiCIAO	vortex	0.6	*H*	1.65	30	79	44.4	ADI
20170312	SCExAO/CHARIS	Lyot	0.5	*JHK*	1.16–2.37	10.32	117	18.5	ADI
20170313	SCExAO/CHARIS	Lyot	0.6	*JHK*	1.16–2.37	14.75	61	25.5	ADI
20180208	SCExAO/CHARIS	Lyot	1.4	*JHK*	1.16–2.37	16.23	12	1.9	SDI
20181128	Keck/NIRC2	Lyot	1.0	$L_{\rm p}$	3.78	30	54	46.3	ADI
20181215	SCExAO/CHARIS	none	⋯	*JHK*	1.16–2.37	20.65	35	34.4	ADI

Note. (a) For CHARIS data, this column refers to the wavelength range. For HiCIAO broadband imaging data, it refers to the central wavelength.

Fontanive et al. 2019; Currie et al. 2020; Bowler et al. 2021; Steiger et al. 2021).

In this paper, we report the direct imaging detection of a low-mass companion at a projected separation of 8 au from the nearby A7IV star, HD 91312 A, using both the Coronagraphic High Angular Resolution Imaging Spectrograph (CHARIS; Groff et al. 2016) behind the Subaru Coronagraphic Extreme Adaptive Optics Project (SCExAO; Jovanovic et al. 2015b) and the NIRC2 camera on Keck. CHARIS spectra and NIRC2 photometry reveal HD 91312 B to be an early-to-mid M dwarf. The HGCA identifies an astrometric acceleration for the primary induced by HD 91312 B; the companion also is responsible for a long-term RV drift identified by Borgniet et al. (2019).

In Section 2, we describe the observations, data reduction, and spectral extraction obtained with SCExAO/HiCIAO, SCExAO/CHARIS, and Keck/NIRC2. In Section 3, we discuss the analysis HD 91312 B. We find that both an empirical spectral comparison and a comparison to atmospheric models find a best match to an early-to-mid M dwarf. An analysis of the Gaia astrometry, orbital motion, and RV trend provides a strong constraint on the mass. Finally, in Section 4, we compare the system to evolutionary models, providing a prediction of the age of the HD 91312 system.

2. Target Properties, Observations, and Data

HD 91312 A is a bright ($M_V = 4.7$) A7IV star located at a distance of 33.28 ± 0.25 pc (Gaia Collaboration et al. 2018). Rhee et al. (2007) identify the star as an IRAS-excess source ($L_{\rm IR}/L_\star \sim 10^{-4}$) consistent with circumstellar dust, although later work has suggested this excess emission results from contamination by an unrelated background object (Bulger et al. 2013). Age estimates for the system vary, from 200 Myr in Rhee et al. (2007) to 700–900 Myr or 19 Myr in David & Hillenbrand (2015) using Bayesian inference and isochrone fitting, respectively.

Previous direct imaging searches failed to identify companions at separations of $\sim 1''$ or greater (e.g., Janson et al. 2013; De Rosa et al. 2014). However, precision RV data identify a long-term trend consistent with an unseen stellar to substellar companion orbiting beyond 5 au from the star (Borgniet et al. 2019). Using the HGCA from Brandt (2018) considering Hipparcos and Gaia-DR2 measurements, we identified a 2.4σ significant astrometric acceleration also consistent with an unseen (sub)stellar companion. Using updated Gaia-eDR3 astrometry, the significance increases to 8.8σ (Brandt et al. 2021, submitted).

High-contrast imaging data for HD 91312 were obtained from SCExAO/CHARIS, Keck/NIRC2, SCExAO/HiCIAO between 2016 December and 2018 December (Table 1). Our Subaru Telescope observations used the HiCIAO infrared camera (Hodapp et al. 2008) in *H*-band ($\lambda_{\rm o} = 1.65$ μm) or the CHARIS integral field spectrograph (Groff et al. 2016) in broadband mode covering *JHK* passbands simultaneously (1.16–2.37 μm, $\mathcal{R} \sim 18$) with SCExAO providing an extreme AO correction. For follow-up observations, we acquired Keck II observations with the NIRC2 camera in the $L_{\rm p}$ broadband filter ($\lambda_o = 3.78$ μm) using Keck's facility AO system.

While conditions were photometric each night, the seeing varied substantially, ranging from $\theta_V = 0.''5$–$0.''6$ for the March 2017 SCExAO/CHARIS data to 1–$1.''4$ for the February and November 2018 SCExAO/CHARIS and Keck/NIRC2 data. Consequentially, the AO performance also varied. Precipitable water vapor levels and the strength of telluric features prominent in channels bracketing the *JHK* passbands for CHARIS also varied.

All CHARIS data utilized satellite spots for precise astrometric and spectrophotometric calibration (e.g., Jovanovic et al. 2015a; Currie et al. 2018), either during (2018 data) or preceding (March 2017) our main sequence of science exposures. Except for the 2018 December epoch, we used a Lyot cornograph with a $0.''23$ diameter occulting spot for all CHARIS observations. The NIRC2 data were taken without a coronagraph. All observations were conducted in "vertical angle"/pupil tracking mode enabling angular differential imaging (ADI; Marois et al. 2006). The CHARIS data also enable spectral differential imaging (SDI; Marois et al. 2000).

The standard CHARIS pipeline (Brandt et al. 2017) extracted data cubes from raw data; the CHARIS postprocessing pipeline developed in Currie et al. (2018) provided basic reduction steps including sky subtraction, image registration, and spectrophotometric calibration. For spectrophotometric calibration, we adopted a Kurucz stellar atmosphere model appropriate for an A7 star. For both the HiCIAO and NIRC2 data, we used a well-tested general purpose high-contrast ADI broadband imaging pipeline (Currie et al. 2010, 2011).

To suppress the stellar halo, we use the least-squares based algorithms—*Adaptive Locally Optimized Combination of Images* (A-LOCI; Currie et al. 2012, 2015) and the *Karhunen-Loè*ve Image Projection (KLIP; Soummer et al. 2012) approaches—in combination with ADI or SDI. We employed more conservative algorithm settings for the highest-quality data sets that also coincide with HD 91312 B's widest angular separation, adopting a high *singular value decomposition* (SVD) cutoff for A-LOCI or truncating the basis set for KLIP at a small number of modes. Due to the poorer seeing, the 2018 epoch data sets suffered from poorer AO performance and

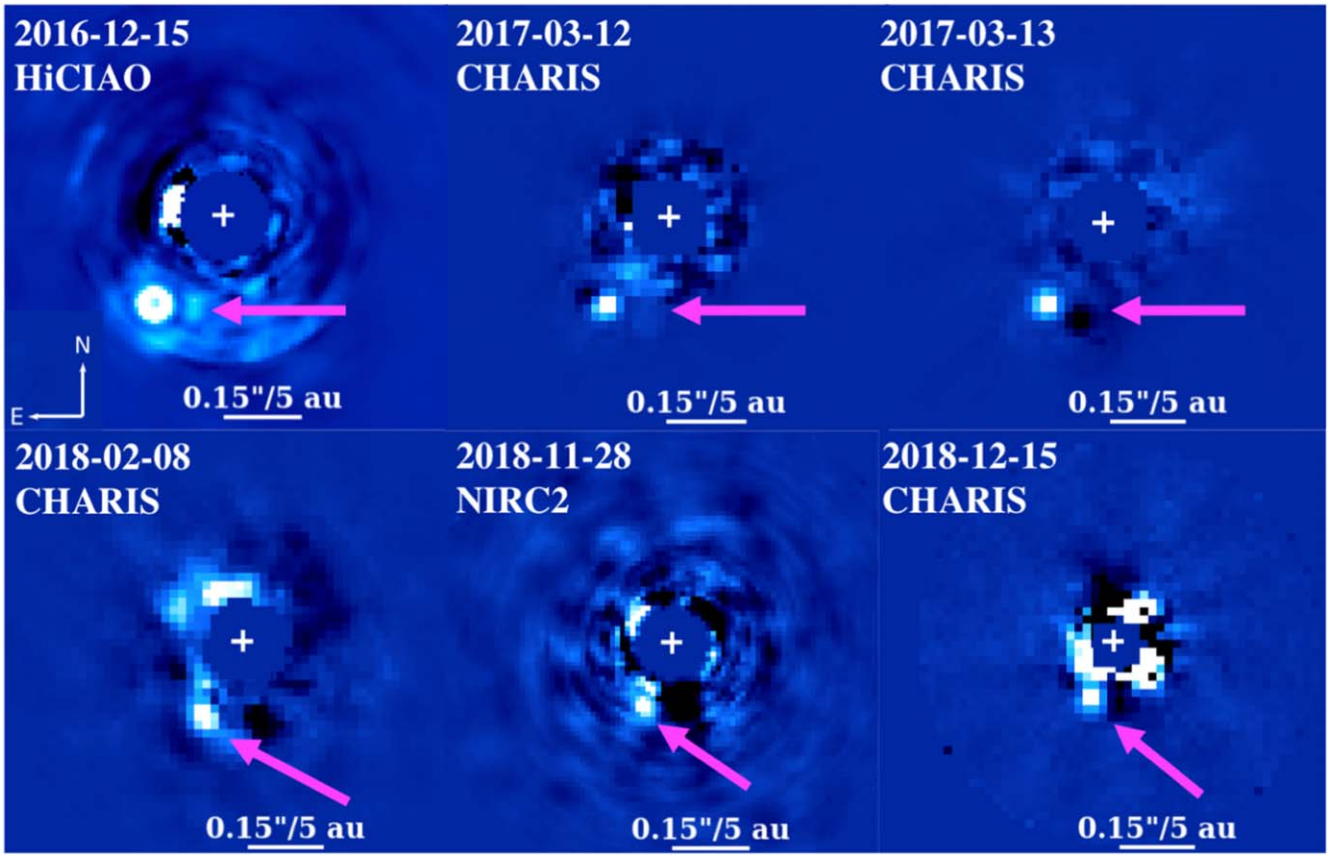

Figure 1. Detections of HD 91312 B (position denoted by the magenta arrow) from 2016 to 2018.

HD 91312 B at a smaller angular separation. For these data, only aggressive approaches—e.g., using A-LOCI in SDI mode or with a small optimization area used to construct a weighted point-source function (PSF; see Lafrenière et al. 2007)—yielded a statistically significant detection. For all the reductions we used an overlap of 0.7 FWHM's. For the March 12 KLIP reduction a KL = 1 was used and for the ALOCI results, we used an SVD limit of 10^{-4} was used. The March 13 ALOCI results used a SVD limit of 10^{-6}.

Figure 1 shows the detection of a faint point-source companion, HD 91312 B, within $\rho \sim 0\farcs2$ of the primary. Even with conservative algorithm settings, the signal-to-noise ratio (S/N) for HD 91312 B's detection obtained with A-LOCI (KLIP) exceeds 68 (37) in the 2017 March 12 data. HD 91312 B's detection significance in the 2017 March 13 data set (37) is a lower limit since a prominent negative self-subtraction footprint counterclockwise from the companion biases the true speckle noise estimate. In the HiCIAO data, HD 91312 B slightly saturates. No data set identifies any additional companion. HD 91312 B appears at smaller angular separations in the 2018 data than in 2016–2017.

3. Analysis

Prior to extracting a spectrum for HD 91312 B and determining the companion's astrometry, we corrected for signal losses due to processing by forward-modeled point sources at HD 91312 B's location using stored coefficients (for A-LOCI) or eigenvectors/eigenvalues (for KLIP) in Currie et al. (2018, 2020) and Pueyo (2016). For CHARIS spectra, we focus on the 2017 March 13 data, as these have a higher throughput and weaker off-diagonal terms in their spectral covariance than the 2017 March 12 data, indicating less spatially/spectrally correlated noise (Greco & Brandt 2016). The 2018 CHARIS epochs have less statistically significant detections, have likewise stronger off-diagonal terms in their spectral covariance, and/or utilized SDI-only for PSF subtraction, which complicates forward modeling (Pueyo 2016).

Our implementation of A-LOCI and KLIP only mildly attenuates HD 91312 B in the 2017 March 13 CHARIS data, as the forward-modeled companion PSF had 85%–95% throughput per channel. In the Keck/NIRC2 data, the aggressive processing needed to achieve a detection yielded far greater signal loss (23% throughput). Except for the Keck/NIRC2 data, we found astrometric biasing to be negligible.

3.1. Common Proper Motion, Orbit, and Dynamical Mass

Table 2 lists HD 91312 B's relative astrometry for each epoch and Figure 2 compares the companion's positions to those expected for a background star. Gaia and Hipparcos provide absolute astrometry of the system, while the direct imaging measurements made with CHARIS, HiCIAO, and NIRC2 provide relative astrometry of the system. The primary exhibits a significant proper motion of $\Delta\alpha$, $\delta \sim -138.1$, -3.2 mas yr^{-1} (Gaia Collaboration et al. 2018). HD 91312 B's astrometry over two years is therefore easily distinguishable from the path of a background star with the primary uncertanty being related to the companion S/N.

Between 2016 December and 2017 March, HD 91312 B's position changes little but its angular separation is substantially smaller in subsequent epochs. This suggests that our earliest

Table 2
HD 91312 B Detection Significance and Astrometry

UT Date	Instrument	S/N[a]	[E, N]($''$)
20161215	SCExAO/HiCIAO	12[b]	[0.133, −0.174] ± [0.007, 0.007]
20170312	SCExAO/CHARIS	68	[0.126, −0.176] ± [0.004, 0.004]
20170313	SCExAO/CHARIS	37[c]	[0.127, −0.172] ± [0.004, 0.004]
20180208	SCExAO/CHARIS	6.3	[0.083, −0.133] ± [0.010, 0.010]
20181128	Keck/NIRC2	3.1	[0.058, −0.122] ± [0.010, 0.020]
20181215	SCExAO/CHARIS	5.3	[0.056, −0.104] ± [0.008, 0.008]

Note. (a) All HD 91312 B S/N estimates draw from reductions used to calculate astrometry. (b) This is a lower limit since HD 91312 B is saturated in HiCIAO images. (c) The S/N is likely underestimated, as negative self-subtraction footprints bias the true speckle noise estimate.

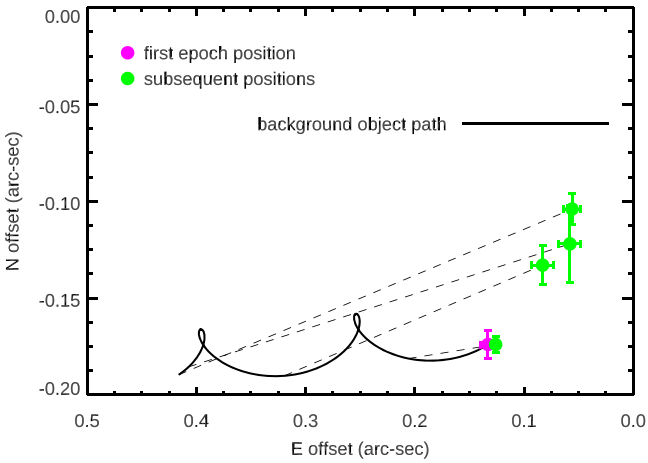

Figure 2. Proper-motion analysis for HD 91312 B. For an initial position measured in 2016 data (magenta dot), the dotted lines connect HD 91312 B's measured position (green dots) to its predicted position were it a background object.

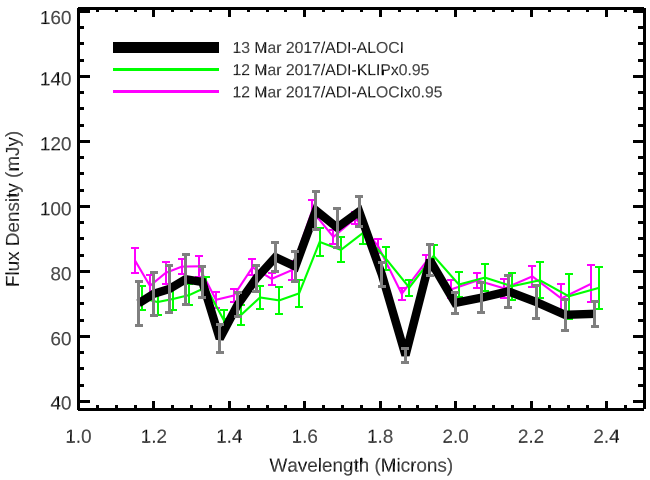

Figure 3. CHARIS spectrum extracted from 2017 March 13 data reduced with ADI/A-LOCI (black thick line, gray error bars) compared to spectra extracted on different nights or with different processing, scaled to roughly match the 2017 March 13 spectrum's absolute flux density level. Errors are drawn from the intrinsic S/N of the detection and the uncertainty in spectrophotometric calibration at that given channel.

epoch detections likely imaged the companion near its maximum projected separation. Visual inspection of Figure 2 shows HD 91312 B at a roughly constant position angle but varying angular separations, suggesting that its orbit is highly inclined along our line-of-sight.

Table 3
HD 91312 B Spectrum

Wavelength (μm)	F_ν (mJy)	σF_ν (mJy)	S/N
1.1596	70.1401	6.7327	10.4178
1.1997	73.0861	6.5475	11.1625
1.2412	74.5914	7.1210	10.4748
1.2842	77.5707	7.6822	10.0975
1.3286	76.7243	4.7999	15.9847
1.3746[a]	59.2881	4.3527	13.6211
1.4222[a]	69.7233	3.6030	19.3515
1.4714	77.8220	3.9974	19.4682
1.5224	84.3496	4.4957	18.7621
1.5750	81.4769	4.6191	17.6391
1.6296	98.7482	5.9409	16.6217
1.6860	93.4650	5.9960	15.5878
1.7443	98.4082	4.6971	20.9508
1.8047	78.9408	3.7200	21.2204
1.8672[a]	54.1538	2.1265	25.4661
1.9318[a]	83.4531	4.7505	17.5671
1.9987	70.2701	3.3121	21.2159
2.0678	71.8675	4.6904	15.3223
2.1394	73.8355	4.9648	14.8718
2.2135	70.5583	5.0372	14.0076
2.2901	66.6173	4.8304	13.7912
2.3693	66.9209	3.8831	17.2340

Note. Throughput-corrected HD 91312 B spectrum extracted from 2017 March 13 data. (a) These spectral channels are likely to be telluric-dominated.

3.2. The Atmosphere of HD 91312 B

The HD 91312 B spectrum shows peaks at J and especially H band characteristic of M- and L-type companions (e.g., Gagné et al. 2015; Figure 3). The 2017 March 13 data show slightly discrepant measurements at 1.85 μm, likely due to that night's stronger telluric emission between J,H,K bands. HD 91312 B's broadband photometry in standard Maunakea Observatory filters derived from the 2017 March 13 CHARIS and 2018 November 28 NIRC2 data is $J = 10.79 \pm 0.10$, $H = 10.13 \pm 0.06$, $K_s = 9.93 \pm 0.07$, and $L_p = 9.79 \pm 0.35$.

In contrast to results for wider-separation companions like HD 33632 Ab (Currie et al. 2020), the spectral covariance at HD 91312 B's location includes substantial off-diagonal terms (Figure 4), especially for spatially-correlated noise ($A_\rho \sim 0.71$). More aggressive ADI processing or employing SDI would reduce the spatially/spectrally correlated noise but would complicate forward modeling and thus impact the fidelity of our extracted spectrum.

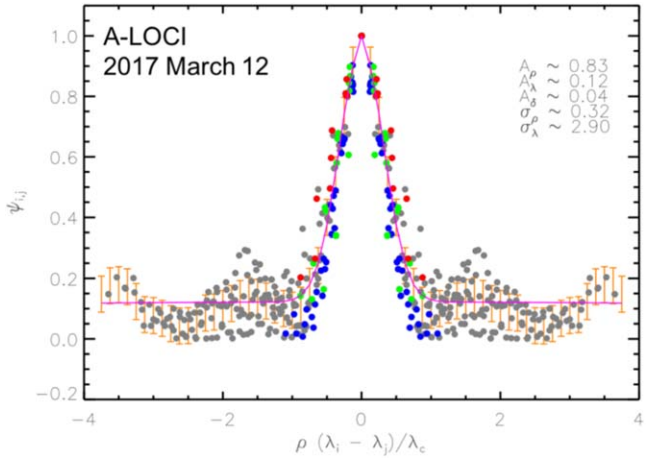

Figure 4. Spectral covariance at the angular separation of HD 91312 B for the A-LOCI-reduced 2017 March 13 data. The magenta line shows our fit to the spectral covariance as a function of scaled separation—$\rho(\lambda_i–\lambda_j)/\lambda_c$—where ρ is the separation in λ/D units for the central wavelength λ_c (see Greco & Brandt 2016). Blue, red, and green circles denote individual measurements between channels within the same major near-IR filter (J, H, or K_s) while gray circles denote other individual measurements. Orange points with error bars denote binned averages with 68% confidence intervals. The channel-independent noise contribution is even smaller for the 2017 March 2017 A-LOCI and KLIP reductions.

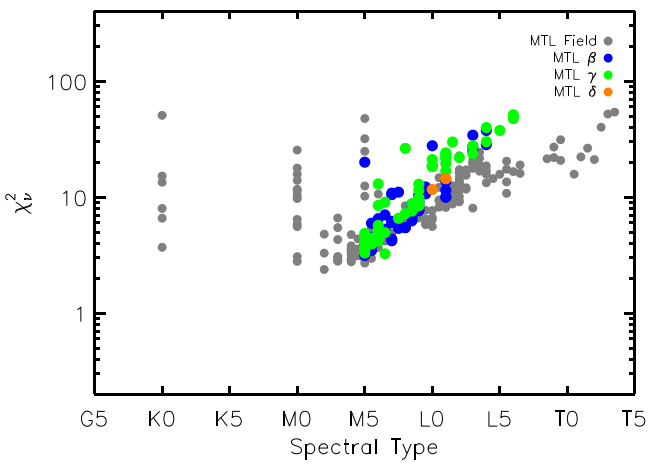

Figure 5. The χ^2_ν vs. spectral type distribution comparing the spectrum of HD 91312 B to those for objects with spectral types between K0 and T5 in the Montreal Spectral Library. Field objects are shown as gray dots. Objects with *very low* (δ), *low* (γ), and *intermediate* (β) gravity classifications are shown as orange, green, and blue dots, respectively.

3.3. Empirical Comparisons to HD 91312 B's Infrared Colors and Spectrum

To empirically constrain HD 91312 B's atmosphere, we first compare its broadband colors to ultracool dwarf colors compiled in Pecaut & Mamajek (2013) and Kenyon & Hartmann (1995), and then its CHARIS spectrum to objects in the Montreal Spectral Library[20] (e.g., Gagné et al. 2014), considering the impact of spatially and spectrally correlated noise (Greco & Brandt 2016). HD 91312 B's $J–H_s$ and $J–K_s$ colors converted to the 2MASS photometric system are 0.72 ± 0.12 and 0.89 ± 0.12 (Pecaut & Mamajek 2013), respectively, which are matched by M5.5–L1 and K7–M7 field objects at the 1σ level, respectively (see Pecaut & Mamajek 2013). Its $J–L_p$ color (0.97 ± 0.35) does not

[20] https://jgagneastro.com/the-montreal-spectral-library/

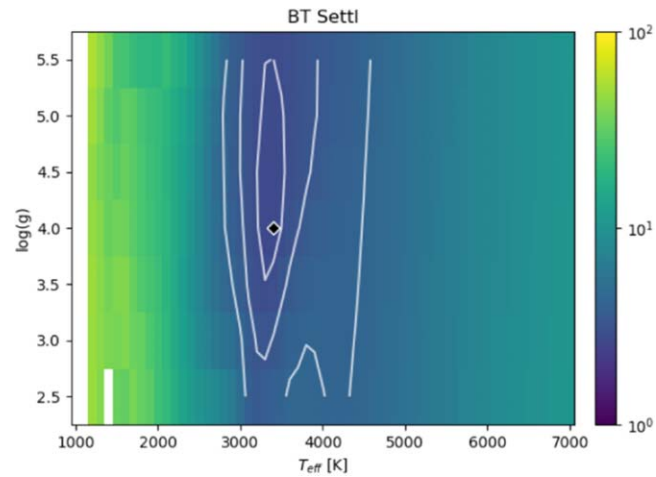

Figure 6. The χ^2_ν fit of the HD 91312 B spectrum to the BT-Settl-CIFIST models (Baraffe et al. 2015) as a function of the model's effective temperature, $T_{\rm eff}$, and $\log(g)$. Fits utilized the Keck L_p-band photometry, along with the CHARIS spectrum from the A-LOCI-reduced 2017 March 13 data, excluding four telluric-dominated spectral channels (those at 1.375, 1.422, 1.867, and 1.932 μm). The best-fit model spectrum (black diamond) has $T_{\rm eff} = 3400$ K and $\log(g) = 4.0$ with a $\chi^2_\nu = 2.75$. Contours show the 1, 3, and 5σ confidence intervals on the χ^2_ν.

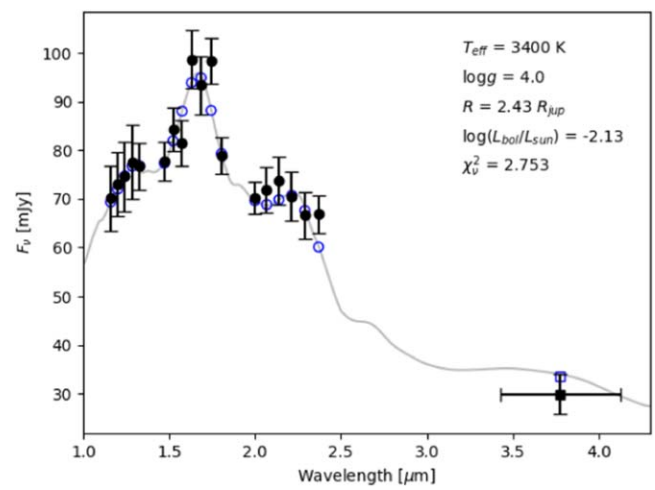

Figure 7. The HD 91312 B spectrum compared to the best-fit BT-Settl-CIFIST model (Baraffe et al. 2015). Model spectrum is shown in gray, smoothed to a spectral resolution of $R = 100$ at 2.5 μm. Binned model spectrum points are denoted as blue open symbols, while the observed HD 91312 B spectrum is shown in black. In both cases, circles indicate points corresponding to the CHARIS spectrum and squares indicate the photometric L_p measurement from Keck. Only spectral points utilized for the model fitting are shown.

well constrain its spectral type (later than K4; Kenyon & Hartmann 1995), due to the large NIRC2 photometric errors.

As shown in Figure 5, HD 91312 B's spectrum is best matched by early-to-mid M dwarfs—M0–M6 objects—which reproduce the H-band peak but otherwise relatively flat spectral shape at J and K_s. Later spectral types tend to have K-band shapes that are too bright and peaked to reproduce HD 91312 B's spectrum. Effective temperatures for M0–M6 dwarfs span $T_{\rm eff} \sim 2850$–3870 K (Pecaut & Mamajek 2013). For M dwarfs, the absolute K-band magnitude and bolometric magnitude correlate well. Adopting the relationship from Casagrande et al. (2008) and assuming a distance of 33.43 pc, HD 91312 B's luminosity is $\log_{10}(L/L_\odot) = -2.09^{+0.12}_{-0.13}$.

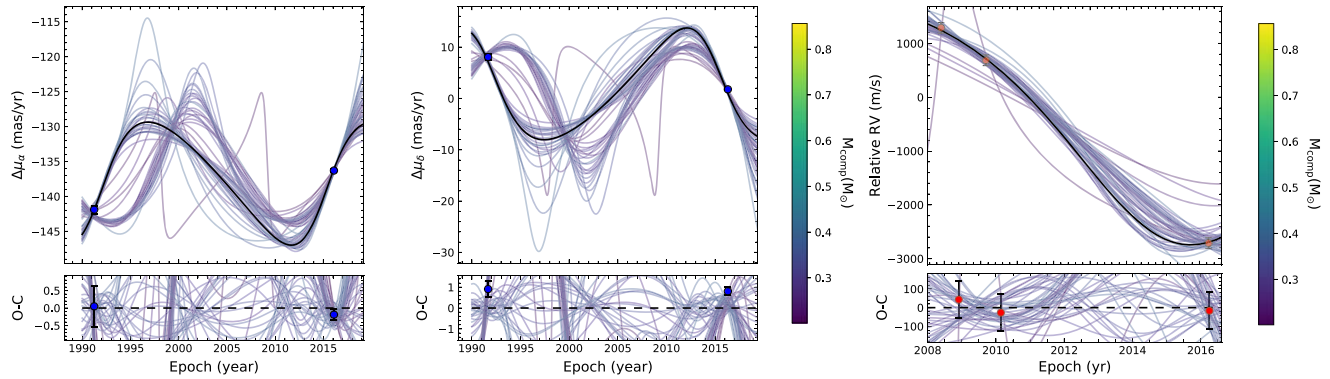

Figure 8. Predicted vs. measured proper-motion acceleration (left, middle panels) and relative radial velocity (right) for HD 91312 A. The curves draw from solutions that jointly fit Hipparcos and Gaia astrometry of HD 91312 A, RV data for HD 91312 A from Borgniet et al. (2019), and relative astrometry of HD 91312 B from CHARIS and NIRC2. Blue and red dots denote measurements; the bottom subpanels show residuals from the best fit (black curve) and others color coded by the dynamical mass of HD 91312 B.

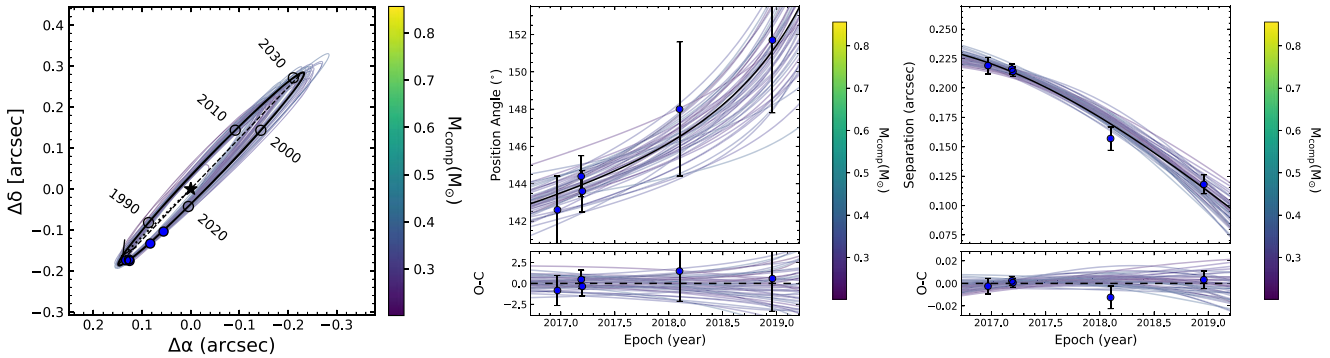

Figure 9. Predicted vs. measured relative astrometry for HD 91312 B. Curves, data points, and subpanels are the same as in Figure 8.

3.4. Atmospheric Model Spectra and HD 91312 B

For comparison to model stellar spectra, we perform a similar fit of HD 91312 B's observed spectrum to the solar metallicity BT-Settl-CIFIST models (Baraffe et al. 2015). As with the previous BT-Settl models (Allard et al. 2012a, 2012b), BT-Settl-CIFIST includes self-consistent cloud formation and sedimentation. However, the latter also includes updated solar abundances and a more detailed treatment of convection (Baraffe et al. 2015). Notably, however, this analysis does not include any constraints on metallicity.

We combine our extracted A-LOCI CHARIS spectrum from 2017 March 13 with the L_p photometric point from NIRC2, ignoring spectral channels that are likely to be telluric-dominated (1.375, 1.422, 1.867, and 1.932 μm in the CHARIS spectrum). As spectra observed with CHARIS are deconvolved from the line-spread function during extraction (Brandt et al. 2017), the model spectra were convolved with a Gaussian corresponding to the appropriate CHARIS spectral bin width at each wavelength (FWHM $= \lambda/R$ converted to spectral bins) and rebinned for comparison with the observed spectra. As the CHARIS spectral resolution is logarithmic in nature, the FWHM of the convolved Gaussian varied as a function of λ across the wavelength range of the CHARIS Broadband filter. To ensure manageable computational time, the same FWHM was used for every 501 model wavelength bins, corresponding to ∼0.15% of the width of the CHARIS Broadband filter. Calculation of the expected model flux in the NIRC2 L_p band used a linear interpolation of NIRC2's L_p bandpass curve provided by the SVO Filter Profile Service (Rodrigo et al. 2012; Rodrigo & Solano 2020).

Once the model spectra have been rebinned to match the observed CHARIS Broadband with NIRC2 L_p photometry, the spectral χ^2_ν is calculated using the same solution to the correlation model of Greco & Brandt (2016) discussed in Section 3.3. The resulting χ^2_ν as a function of model $T_{\rm eff}$ and $\log g$ is shown in Figure 6. Our spectroscopic/photometric measurements are best fit by the BT-Settl-CIFIST model with $T_{\rm eff} = 3400$ K and $\log g = 4.0$, resulting in $\chi^2_\nu = 2.75$. This best-fit model spectrum, shown with the observed data in Figure 7, results in a radius of $R = 2.43 \pm 0.05 R_{\rm Jup}$ and a $\log_{10}(L_{\rm bol}/L_{\rm Sun}) = -2.13^{+0.03}_{-0.04}$. Noteably, the 1σ confidence interval on the χ^2_ν fit does not provide strong constraints on $\log g$ (see Figure 6), ranging from $\log g = 3.5$–5.5. However, the effective temperatures that fall within the 1σ (3σ) confidence interval indicate a spectral type of ∼M2–4 (M5.5–K9), with the best-fit $T_{\rm eff} = 3400$ K model corresponding with a spectral type of ∼M3 (Pecaut & Mamajek 2013).

3.5. Astrometry

We use the open-source code orvara (Brandt et al. 2021) to fit the low-mass companion of HD 91312. The mass and orbit are fit using a combination of the Hipparcos and Gaia Catalogues, RV measurements from (Borgniet et al. 2019), and relative astrometry from SCExAO/HiCIAO, SCExAO/CHARIS and Keck/NIRC2. We fit for the mass of the primary and companion, the semimajor axis, the eccentricity, and inclination. We assume that the companion observed is solely

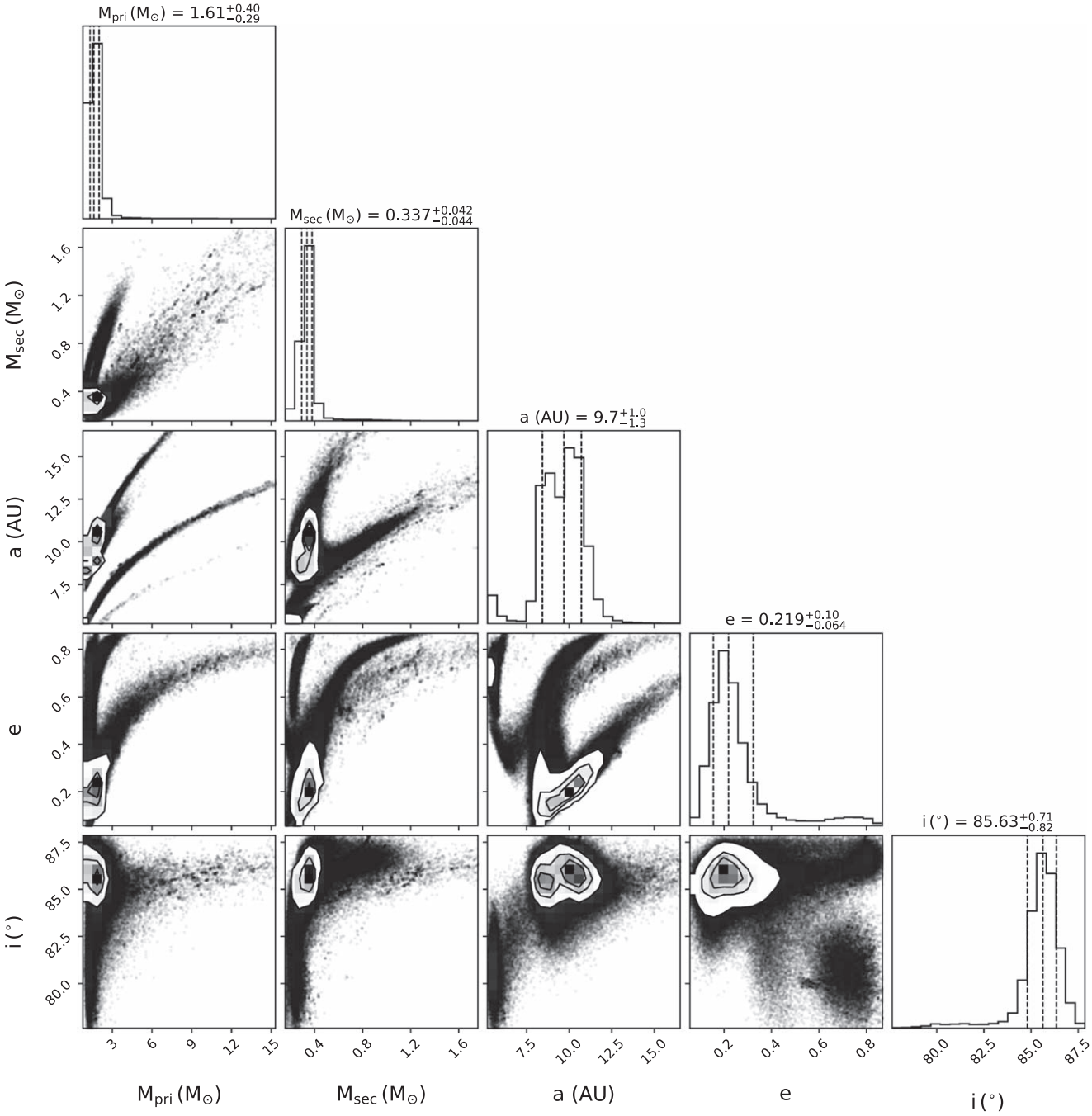

Figure 10. Posterior distributions of selected orbital parameters for HD 91312 B.

responsible for the acceleration observed in between the Hipparcos and Gaia catalogs. For the fit, we assume lognormal priors on mass and semimajor axis, a geometric prior on inclination, a Gaussian prior on parallax using the Gaia EDR3 measurement and its uncertainty, and uniform priors on the remaining parameters. The code analytically marginalizes out parallax, barycenter proper motion, and barycenter radial velocity as nuisance parameters. A full description of orvara and its available parameters can be found in Brandt et al. (2021). Figure 8 shows the predicted versus measured proper-motion acceleration and relative radial velocity for HD 91312 A and Figure 9 shows the predicted versus measured relative astrometry for HD 91312 B. The companion has a best-fit mass of $0.337^{+0.042}_{-0.044}$ $M_\odot$ with a best-fit semimajor axis of $9.7^{+1.0}_{-1.3}$ au and an orbital inclination of $i = 85.63^{+0.71}_{-0.82}$ degrees. Figure 10 shows our posterior distribution of selected orbital parameters.

4. Comparison to Stellar Evolution Models

To obtain an age estimate, we compared the derived $T_{\rm eff}$ and luminosity of the HD 91312 AB system to isochrones from several stellar evolution grids. This analysis was performed with the Dartmouth (Dotter et al. 2008; Feiden et al. 2011), Yale-Potsdam Stellar Isochrones (YaPSI; Spada et al. 2017), MESA Isochrones and Stellar Tracks (MIST; Choi et al. 2016; Dotter 2016) utilizing the Modules for Experiments in Stellar Astrophysics (MESA) code (Paxton et al. 2011, 2013, 2015, 2018), and the BHAC15 (Baraffe et al. 2015) evolutionary models.

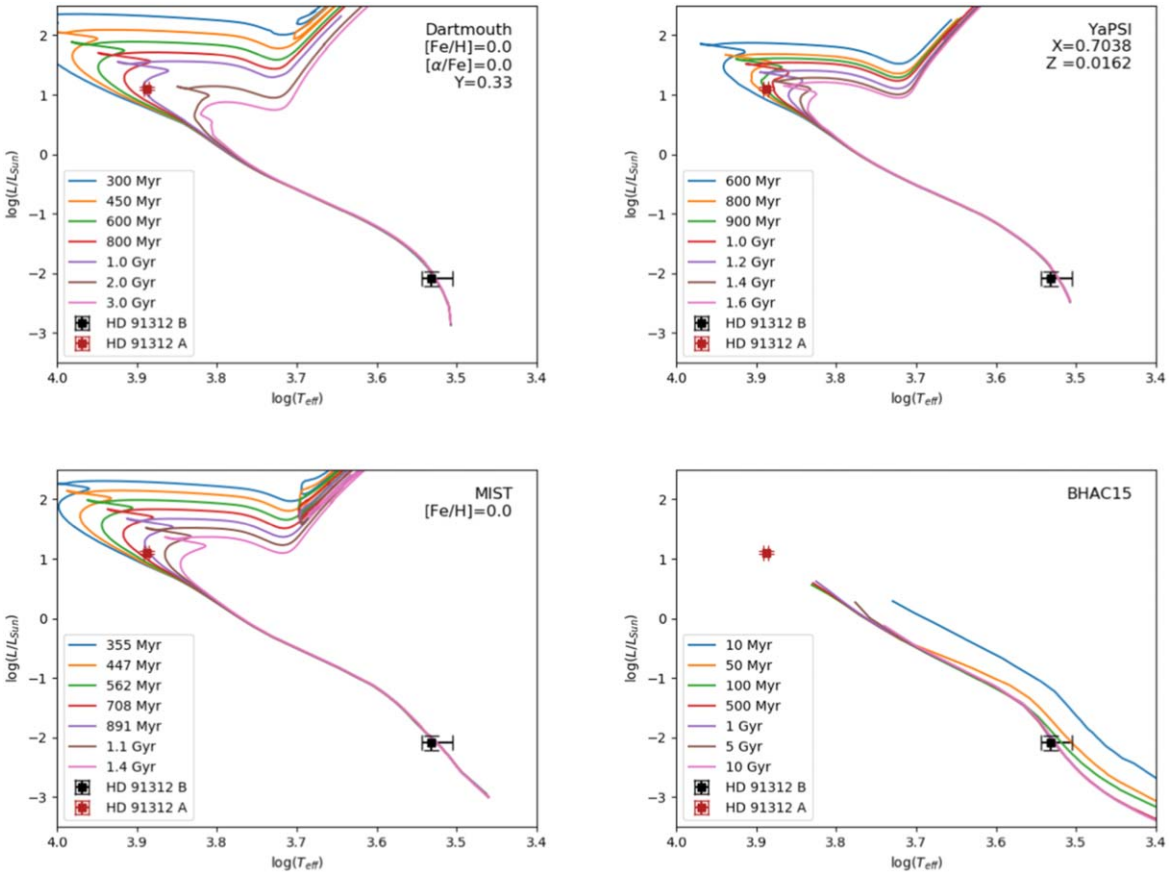

Figure 11. HD 91312 A and B plotted with isochrones at select ages from several stellar evolution grids. The Dartmouth, YaPSI, and MIST isochrones shown are the models closest to solar composition of those that are consistent with the $\log(L/L)$ and $\log T_{\rm eff}$ of both HD 91312 A and B. The MIST model shown has $v/v_{\rm crit} = 0.4$. BHAC15 isochrones are not differentiated by composition.

For the Dartmouth, YaPSI, and MIST models, we consider only isochrones that are simultaneously consistent with the $\log_{10}(L/L_\odot)$ and $T_{\rm eff}$ of HD 91312 A and B within 1σ. For HD 91312 B, we use the $T_{\rm eff} = 3400^{+100}_{-200}$ K from Section 3.4 with the empirical $\log_{10}(L/L_\odot) = -2.09^{+0.12}_{-0.13}$ (Section 3.3). While the empirical and modeled bolometric luminosities derived in Sections 3.3 and 3.4 are consistent within their uncertainties, the uncertainties derived from model fitting do not include the uncertainties in the model spectra, themselves. Therefore, we use the empirical bolometric luminosity in this stellar evolution analysis for a more complete representation of the uncertainty. For HD 91312 A, we use $\log T_{\rm eff} = 3.888 \pm 0.003$ and $\log_{10}(L/L_\odot) = 1.1040 \pm 0.0178$ from Zorec & Royer (2012). We perform a similar analysis with the BHAC15 models using only the data for HD 91312 B, as HD 91312 A is beyond the mass limits of their models (0.07–1.4 $M_\odot$; Baraffe et al. 2015). Example isochrones from each model at or near stellar metallicity are shown in Figure 11.

For each isochrone that is simultaneously consistent with HD 91312 A and B (or B alone, in the case of the BHAC15 models), we estimate the range of masses for each source that lie along the isochrone within 1σ of the measured $\log_{10}(L/L_\odot)$ and $T_{\rm eff}$ for the source. Figure 12 provides a more detailed view of the allowed mass range for each source as a function of isochrone age and, in the cases of the Dartmouth, YaPSI, and MIST models, metallicity.

When combined with the astrometric mass for HD 91312 B derived in Section 3.5, the system becomes inconsistent with the lowest-metallicity Dartmouth ([Fe/H] < -1.0), YaPSI ($Z < 0.01$) models, and MIST ([Fe/H] < 0.0) models. Figure 13 shows the full range of ages and masses for each source allowed by each of the four stellar evolution grids, both before and after constraining the mass ranges for HD 91312 A and B to be within 1σ of the astrometric masses. With no mass constraints, the 1σ age ranges given by each model are 0.35–2.5 Gyr (Dartmouth AB), 0.6–1.6 Gyr (YaPSI AB), 0.45–1.3 Gyr (MIST AB), and 0.04–10 Gyr (BHAC15 B). Imposing the mass constraints reduces the allowed age ranges to 0.35–1.5 Gyr (Dartmouth AB), 0.6–1.4 Gyr (YaPSI AB), 0.45–1.0 Gyr (MIST AB), and 0.2–10 Gyr (BHAC15 B).

5. Conclusions and Discussion

In this work, we directly image and characterize a low-mass stellar companion to the A7 star HD 91312 with SCExAO/CHARIS, SCExAO/HiCIAO, and Keck/NIRC2. The presence of HD 91312 B is consistent with a long-term radial-velocity trend seen by ground-based Doppler surveys (Borgniet et al. 2019) and space-based precision astrometry missions (Brandt 2018; Gaia Collaboration et al. 2018).

HD 91312 B's spectrum is best matched by early-to-mid M-dwarf spectra. Modeling the SCExAO/CHARIS spectrum and $L_{\rm p}$ photometry from Keck/NIRC2 using the BT-Settl-CIFIST models yields a best fit to a 3400^{+100}_{-200} K object with a $\log(g) = 4.0^{+1.5}_{-0.5}$, consistent with empirical comparisons. Combining relative astrometry of HD 91312 B with radial-velocity measurements and absolute astrometry of the star yields a dynamical mass

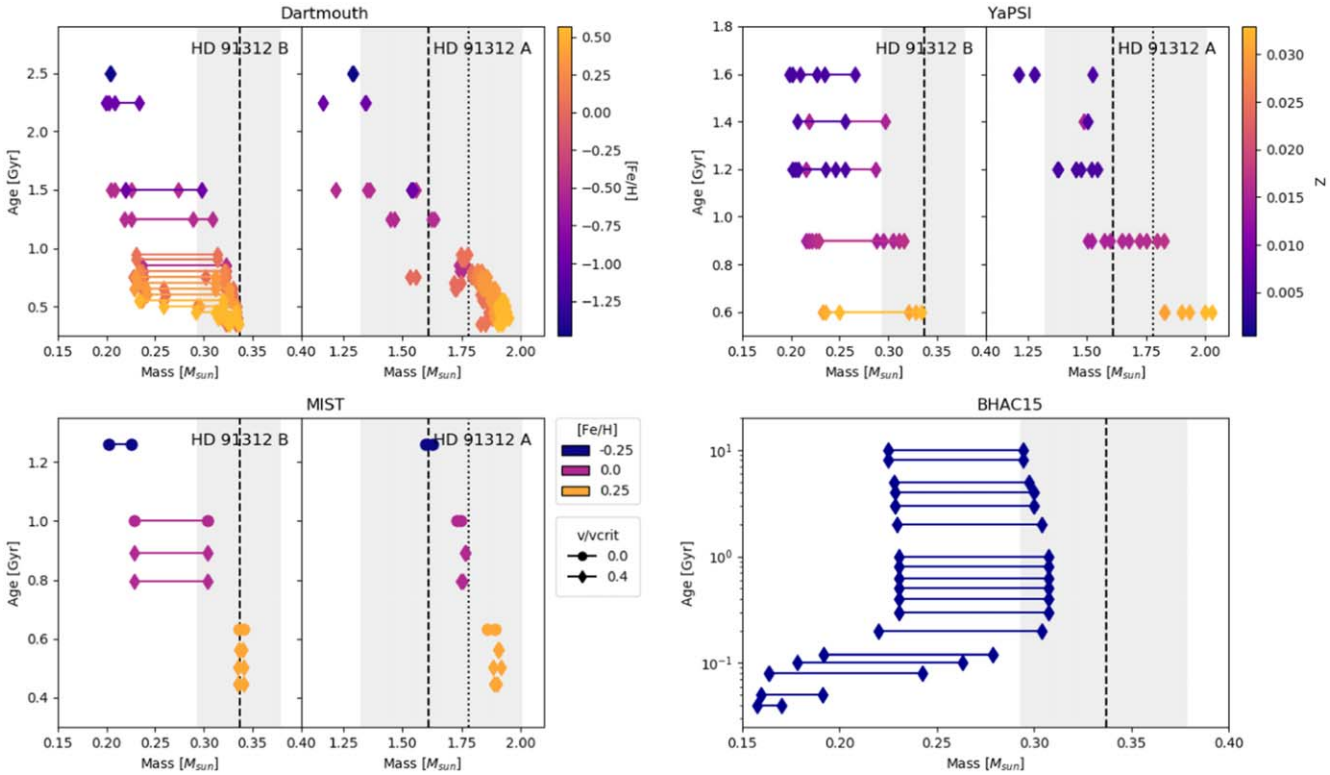

Figure 12. System age vs. mass as derived from several stellar evolution models. For the Dartmouth, YaPSI, and MIST models, masses shown were derived from luminosity-$T_{\rm eff}$ isochrones consistent with both HD 91312 A and B within the 1σ uncertainties. Mass ranges are shown for both sources. The Baraffe et al. models do not extend to the mass of HD 91312 A, so the ages shown are derived from isochrones consistent with HD 91312 B, alone. The dashed black line and gray shading indicate the astrometric masses derived in Section 3.5 and their uncertainty, respectively. The dotted black line indicates the HD 91312 A mass from Zorec & Royer (2012).

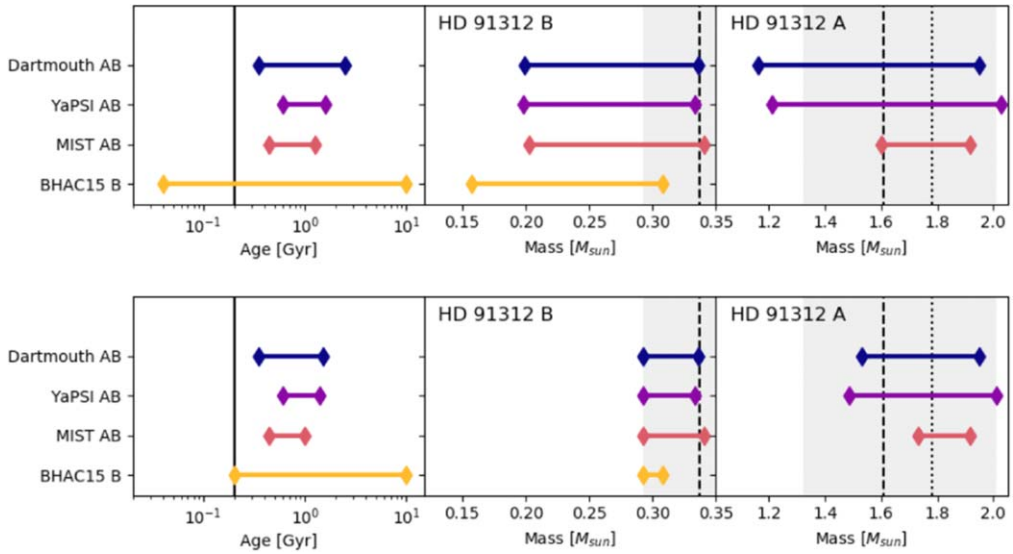

Figure 13. Overview of the consistent age and mass ranges from all isochrone fits with no mass constraints (top) and after constraining by the astrometric masses in Section 3.5 (bottom). Both figures give the range of allowed stellar ages (left) as well as the mass ranges for HD 91312 B (center) and A (right) from all isochrone fits. Model name is labeled to the left, along with whether the fits were performed with both 91312 A and B or B alone. The solid black line denotes the age of HD 91312 A as derived by Rhee et al. (2007). The dashed black lines with shading in the center and right figures indicate the astrometric mass and uncertainty, respectively derived in Section 3.5. The dotted black line shows the mass of 91312 A from Zorec & Royer (2012).

for the companion of $0.337^{+0.042}_{-0.044}$ $M_{\odot}$, also consistent with the results from spectral fitting. To obtain an age estimate of the HD 91312 AB system, we derived $T_{\rm eff}$ and luminosity and compared these to isochrones from several stellar evolution grids. While specific constraints vary, the Dartmouth, YaPSI, and MIST models for the 91312 AB system predict an age between ∼0.35 and 1.5 Gyr when including astrometric mass, and are, in general, inconsistent with the lowest-metallicity models.

The combination of direct imaging with indirect methods provides a clearer picture of the HD 91312 system. Absent

dynamical mass information from astrometry and radial velocity, the mass for HD 91312 B would have to have been inferred from luminosity evolution models assuming a system age, which is not tightly constrained. The inclusion of data from these indirect methods, however, yields a mass precision of ∼10%. Finally, this result with other companions discovered from our Hipparcos–Gaia direct imaging survey reinforce the value of using astrometry to screen for promising direct imaging targets (Currie et al. 2020; Steiger et al. 2021). The revised version of HGCA uses Gaia-eDR3 astrometry, which is about a factor of 3 more precision than that in the DR2 release (Brandt et al. 2021, submitted), making the catalog more sensitive to the presence of Jovian companions. The first joint direct imaging + astrometry discovery of an exoplanet is likely only a matter of time.

We thank the anonymous referee for helpful comments that improved the quality of this paper. The authors wish to acknowledge the very significant cultural role and reverence that the summit of Maunakea holds within the indigenous Hawaiian community. We are most fortunate to have the opportunity to conduct observations from this mountain.

We wish to acknowledge the critical importance of the current and recent Subaru and Keck Observatory daycrew, technicians, telescope operators, computer support, and office staff employees. Their expertize, ingenuity, and dedication is indispensable to the continued successful operation of these observatories.

T.C. was supported by a NASA Senior Postdoctoral Fellowship and NASA/Keck grant LK-2663-948181. We thank the Subaru and NASA Keck Time Allocation Committees for their generous support of this program.

The development of SCExAO was supported by JSPS (Grant-in-Aid for Research #23340051, #26220704 & #23103002), Astrobiology Center of NINS, Japan, the Mt Cuba Foundation, and the director's contingency fund at Subaru Telescope. CHARIS was developed under the support by the Grant-in-Aid for Scientific Research on Innovative Areas #2302. Some of the data presented herein were obtained at the W. M. Keck Observatory, which is operated as a scientific partnership among the California Institute of Technology, the University of California and the National Aeronautics and Space Administration. The Observatory was made possible by the generous financial support of the W. M. Keck Foundation.

K.W. acknowledges support from NASA through the NASA Hubble Fellowship grant HST-HF2-51472.001-A awarded by the Space Telescope Science Institute, which is operated by the Association of Universities for Research in Astronomy, Incorporated, under NASA contract NAS5-26555.

M.T. is supported by JSPS KAKENHI grant Nos.18H05442, 15H02063, and 22000005.

This work was supported by JSPS Grants-in-Aid for Scientic Research, 17K05399 (E.A.).

ORCID iDs

Jeffrey Chilcote https://orcid.org/0000-0001-6305-7272
Taylor Tobin https://orcid.org/0000-0001-8103-5499
Thayne Currie https://orcid.org/0000-0002-7405-3119
Timothy D. Brandt https://orcid.org/0000-0003-2630-8073
Masayuki Kuzuhara https://orcid.org/0000-0002-4677-9182
Olivier Guyon https://orcid.org/0000-0002-1097-9908
Julien Lozi https://orcid.org/0000-0002-3047-1845
Nemanja Jovanovic https://orcid.org/0000-0001-5213-6207
Ananya Sahoo https://orcid.org/0000-0003-2806-1254
Vincent Deo https://orcid.org/0000-0003-4514-7906
Eiji Akiyama https://orcid.org/0000-0002-5082-8880
Markus Janson https://orcid.org/0000-0001-8345-593X
Jungmi Kwon https://orcid.org/0000-0003-2815-7774
Michael W. McElwain https://orcid.org/0000-0003-0241-8956
Jun Nishikawa https://orcid.org/0000-0001-9326-8134
Kevin Wagner https://orcid.org/0000-0002-4309-6343
Krzysztof Hełminiak https://orcid.org/0000-0002-7650-3603
Nour Skaf https://orcid.org/0000-0002-9372-5056
Motohide Tamura https://orcid.org/0000-0002-6510-0681

References

Allard, F., Homeier, D., & Freytag, B. 2012, RSPTA, 370, 2765
Allard, F., Homeier, D., Freytag, B., & Sharp, C. M. 2012, in EAS Publications Series Vol. 57, ed. C. Reylé, C. Charbonnel, & M. Schultheis (Les Ulis: EDP Sciences), 3
Baraffe, I., Homeier, D., Allard, F., & Chabrier, G. 2015, A&A, 577, A42
Barman, T. S., Konopacky, Q. M., Macintosh, B., & Marois, C. 2015, ApJ, 804, 61
Berardo, D., Cumming, A., & Marleau, G.-D. 2017, ApJ, 834, 149
Blunt, S., Nielsen, E. L., De Rosa, R. J., et al. 2017, AJ, 153, 229
Borgniet, S., Lagrange, A. M., Meunier, N., et al. 2019, A&A, 621, A87
Bowler, B. P., Cochran, W. D., Endl, M., et al. 2021, AJ, 161, 106
Brandt, T. D. 2018, ApJS, 239, 31
Brandt, T. D., Dupuy, T. J., & Bowler, B. P. 2019, AJ, 158, 140
Brandt, T. D., Dupuy, T. J., Li, Y., et al. 2021, AJ, 162, 186
Brandt, T. D., Rizzo, M., Groff, T., et al. 2017, JATIS, 3, 048002
Bulger, J., Hufford, T., Schneider, A., et al. 2013, A&A, 556, A119
Calissendorff, P., & Janson, M. 2018, A&A, 615, A149
Carson, J., Thalmann, C., Janson, M., et al. 2013, ApJL, 763, L32
Casagrande, L., Flynn, C., & Bessell, M. 2008, MNRAS, 389, 585
Choi, J., Dotter, A., Conroy, C., et al. 2016, ApJ, 823, 102
Currie, T., Bailey, V., Fabrycky, D., et al. 2010, ApJL, 721, L177
Currie, T., Brandt, T. D., Kuzuhara, M., et al. 2020, ApJL, 904, L25
Currie, T., Brandt, T. D., Uyama, T., et al. 2018, AJ, 156, 291
Currie, T., Burrows, A., Itoh, Y., et al. 2011, ApJ, 729, 128
Currie, T., Cloutier, R., Brittain, S., et al. 2015, ApJL, 814, L27
Currie, T., Debes, J., Rodigas, T. J., et al. 2012, ApJL, 760, L32
David, T. J., & Hillenbrand, L. A. 2015, ApJ, 804, 146
De Rosa, R. J., Patience, J., Wilson, P. A., et al. 2014, MNRAS, 437, 1216
Dotter, A. 2016, ApJS, 222, 8
Dotter, A., Chaboyer, B., Jevremović, D., et al. 2008, ApJS, 178, 89
Feiden, G. A., Chaboyer, B., & Dotter, A. 2011, ApJL, 740, L25
Fontanive, C., Mužić, K., Bonavita, M., & Biller, B. 2019, MNRAS, 490, 1120
Gagné, J., Faherty, J. K., Cruz, K. L., et al. 2015, ApJS, 219, 33
Gaia Collaboration, Brown, A. G. A., Vallenari, A., et al. 2018, A&A, 616, A1
Gagné, J., Lafrenière, D., Doyon, R., Malo, L., & Artigau, É. 2014, ApJ, 783, 121
Greco, J. P., & Brandt, T. D. 2016, ApJ, 833, 134
Groff, T. D., Chilcote, J., Kasdin, N. J., et al. 2016, Proc. SPIE, 9908, 99080O
Hodapp, K. W., Suzuki, R., Tamura, M., et al. 2008, Proc. SPIE, 7014, 701419
Janson, M., Brandt, T. D., Moro-Martín, A., et al. 2013, ApJ, 773, 73
Jovanovic, N., Guyon, O., Martinache, F., et al. 2015a, ApJL, 813, L24
Jovanovic, N., Martinache, F., Guyon, O., et al. 2015b, PASP, 127, 890
Kenyon, S. J., & Hartmann, L. 1995, ApJS, 101, 117
Kuzuhara, M., Tamura, M., Kudo, T., et al. 2013, ApJ, 774, 11
Lafrenière, D., Marois, C., Doyon, R., Nadeau, D., & Artigau, É. 2007, ApJ, 660, 770
Lagrange, A. M., Boccaletti, A., Langlois, M., et al. 2019, A&A, 621, L8
Lagrange, A. M., Rubini, P., Nowak, M., et al. 2020, A&A, 642, A18
Marois, C., Doyon, R., Racine, R., & Nadeau, D. 2000, PASP, 112, 91
Marois, C., Lafrenière, D., Doyon, R., Macintosh, B., & Nadeau, D. 2006, ApJ, 641, 556
Marois, C., Macintosh, B., Barman, T., et al. 2008, Sci, 322, 1348
Nakajima, T., Oppenheimer, B. R., Kulkarni, S. R., et al. 1995, Natur, 378, 463
Paxton, B., Bildsten, L., Dotter, A., et al. 2011, ApJS, 192, 3

Paxton, B., Cantiello, M., Arras, P., et al. 2013, ApJS, 208, 4
Paxton, B., Marchant, P., Schwab, J., et al. 2015, ApJS, 220, 15
Paxton, B., Schwab, J., Bauer, E. B., et al. 2018, ApJS, 234, 34
Pecaut, M. J., & Mamajek, E. E. 2013, ApJS, 208, 9
Pueyo, L. 2016, ApJ, 824, 117
Rhee, J. H., Song, I., Zuckerman, B., & McElwain, M. 2007, ApJ, 660, 1556
Rodrigo, C., & Solano, E. 2020, Contributions to the XIV.0 Scientific Meeting (virtual) of the Spanish Astronomical Society (Almería: Spanish Astronomical Society), 182
Rodrigo, C., Solano, E., & Bayo, A. 2012, SVO Filter Profile Service Version 1.0, IVOA Working Draft 15 October 2012
Soummer, R., Pueyo, L., & Larkin, J. 2012, ApJL, 755, L28
Spada, F., Demarque, P., Kim, Y. C., Boyajian, T. S., & Brewer, J. M. 2017, ApJ, 838, 161
Spiegel, D. S., & Burrows, A. 2012, ApJ, 745, 174
Steiger, S., Currie, T., Brandt, T. D., et al. 2021, AJ, 162, 44
Zimmerman, N., Oppenheimer, B. R., Hinkley, S., et al. 2010, ApJ, 709, 733
Zorec, J., & Royer, F. 2012, A&A, 537, A120